ADVANCED FUNCTIONAL MATERIALS
www.afm-journal.de

Magnetic Colloidal Currents Guided on Self-Assembled Colloidal Tracks

José Martín-Roca, Francisco Ortega, Chantal Valeriani, Ramón González Rubio, and Fernando Martínez-Pedrero**

The nondiffusive directional transport of micro-cargos, such as colloids, cells, or liposomes, is vital for living organisms, for example in the intracellular transport of cytoplasmic organelles along actin filaments or microtubules, and also in numerous applications in biomedicine and nanotechnology. Mimicking natural designs, the self-assembly capacity of magnetic colloids is studied and exploited to construct different paths along which swarms of magnetic micro/nanoparticles can be guided. Driven transport is possible thanks to the combined effect of the magnetic microstructure of the self-assembled tracks, adsorbed on a solid interface, and the application of a time-dependent magnetic field. Nonadsorbed magnetic particles propel along the pre-formed structures under the action of an externally controllable traveling potential ratchet, like molecular walkers. The transport mechanisms are determined by both the properties of the particles and the configuration of the applied field. Finally, it is shown how the proposed combination of self-assembly and guided transport paves the way to the development of a new class of techniques, able to adapt ad hoc to the environment, and transport of microparticles along irregular profiles and/or crowded conditions. The technological interest is immediate, including drug delivery and controlled guidance of microcargos, in biological environments and microfluidic platforms.

1. Introduction

One of the main goals of today technology is building micrometer-scale robots with reliable performance, that might lead to new applications, for instance in bio-detection, theragnosis, drug delivery, single-cell manipulation, microsurgery filtration, molecular separation, size analysis, or point-of-care diagnostics.[1,2] Fully functional small-scale actuated robots are often designed at a millimeter scale.[3] However, at smaller length scales actuation becomes more difficult to achieve, since directed transport through a viscous fluid is limited by the effect of thermal fluctuations, the constraint imposed by the scallop theorem, and the presence of external flows, obstacles, confinements, and/or interfaces.[4] Non-diffusive transport of micro-cargoes, such as colloids, cells, microcapsules, or liposomes, through a viscous fluid is not only crucial for numerous applications in biomedicine and nanotechnology, but also vital for fundamental aspects of living organisms. For example, dynein, myosin, and kinesin molecular walkers, -which are essential to intracellular transport, cell motility, spindle assembly, and chromosome segregation during cell division- actively drag vesicles and organelles along dynamic-self-assembled microtubules.[5,6] These cytoskeleton proteins use the energy from ATP hydrolysis either to walk on the binding sites of microtubules, with the help of one or two binding groups connected with a flexible joint or to regulate microtubule dynamics, result of the polymerization and depolymerization of α- and β-tubulin heterodimers. Molecular motors can be engineered to reversibly change their direction of motion,[7] and the process can be replicated in vitro, with kinesin-coated particles actively moving along immobilized

J. Martín-Roca, C. Valeriani
Departamento de Estructura de la Materia
Física Térmica y Electrónica
Universidad Complutense de Madrid
28040 Madrid, Spain
E-mail: josema10@ucm.es

The ORCID identification number(s) for the author(s) of this article can be found under https://doi.org/10.1002/adfm.202306541

DOI: 10.1002/adfm.202306541

J. Martín-Roca, C. Valeriani
GISC-Grupo Interdisciplinar de Sistemas Complejos
Departamento de Estructura de la Materia, Física Térmica y Electrónica
28040 Madrid, Spain

F. Ortega, R. G. Rubio, F. Martínez-Pedrero
Departamento de Química-Física
Universidad Complutense de Madrid
Avda. Complutense s/n, 28040 Madrid, Spain
E-mail: fernandm@ucm.es

F. Ortega, R. G. Rubio, F. Martínez-Pedrero
Inst. Pluridisciplinar
Universidad Complutense de Madrid
Paseo Juan 23,1, E-28040 Madrid, Spain

microtubules.[8] To achieve directional transport at the molecular scale, scientists have created ways to mimic motor proteins that can walk along pathways.[9]

Direct transport of micro-cargos in a viscous medium has traditionally been mainly explored using strategies based on the local generation of stable hydrodynamic flows or the generation of traveling potentials.[10] In the first set of approaches, microorganisms or catalyzed Janus particles propel through the viscous fluid by generation of uncompensated hydrodynamic stresses along the surface of the swimmer. These hydrodynamic flows can also be generated with the help of controlled fields, that force individual particles or induced self-assemblies into rotational or oscillatory motions. Such motions become translational through the imposed breaking of symmetry.[11] In these strategies, the transport mechanism can also be favored by the hydrodynamic interactions with micro-structured substrates.[12] However, the use of strategies based on the generation of stable flow patterns is sometimes limited or hindered by the concurrence of other complex flow environments, such as cardiovascular flows, or increased viscoelasticity in physiological fluids, especially at the nanoscale.[13] In the second set of approaches, particles are driven by actuated optical lattices[14] or micro-structured substrates, which generate time-dependent energy landscapes. For instance, Skaug et al.[1] created different 3D topographies that generate an asymmetric static potential landscape, in which nanoparticles are driven and sorted by the action of externally applied non-equilibrium fluctuations. Similarly, magnetic microparticles can perform adiabatic transport when floating on some specific substrates, such as ferromagnetic garnet films or lithographic surfaces.[15,16] These engineered substrates are composed of regions with different magnetizations that can be energized by a time-dependent magnetic field. Inspired by the above strategy, recent advances have tried to combine self-assembly and propulsion, by using tiny building blocks to generate the micropatterns along which currents of micro-particles are driven.[17,18] So far, however, all the proposed strategies require the combination of strong confinement, or the use of substrates limited in their reconfigurability, making them incompatible with most applications.[16,17,19]

At the same time, magnetic micro- or nanoparticles with tunable size, shape, and interactions were also used as model systems to understand the physical mechanisms controlling static and dynamic self-assembly.[20] In processes leading to static self-assemblies, the system tends to reversibly reach local or global minima of free energy, and Brownian colloids, like real atoms, form different patterns. Examples of static self-assemblies composed of magnetic colloidal particles range from chains, to bundles, rings, stair-like structures, or 2D crystals and glasses.[21,22] On the other hand, in dynamic self-assembling the system continuously dissipates an energy that plays a relevant role in the main features of the out-of-equilibrium structures. Examples of dynamic self-assemblies composed of magnetic colloidal particles range from worms, square-like structures, and carpets to sheets of superparamagnetic colloids, or staggered head-to-tail chains.[21,23] The final spatial arrangement is strongly determined not only by the size, shape, and magnetic character of the composing particles (susceptibility, coercivity...), but also by the features of the applied field (amplitude, frequency, ellipticity...).[24] Alternatively, magnetic colloids can bind through binding molecules to form smart colloidal polymers, that were designed in the past as synthetic micromixers, cilia, and flagella.[25,26]

In this work, we use the ability of magnetic suspensions to self-assemble into a variety of transient superstructures to construct immobile assemblies upon which other mobile magnetic colloids can be driven. Once adsorbed on a solid substrate, the engineered structures serve as highways for the synchronous and asynchronous transport of magnetic colloids, when both the spatial magnetic micro-structure of the formed tracks and the application of a time-dependent magnetic field allows for the generation of a traveling potential. By tracking the position of magnetic particles of different micro/nano sizes, we first explore the different transport mechanisms, that allow particles, dimers, trimers, or disc-shaped aggregates to be transported on the self-assembled tracks. The supporting mechanism is strongly determined by the relative size of the cargos/rail units, as well as by the strength, orientation, ellipticity, and frequency of the applied field. The proposed strategy is also tested in microfluidic channels, featuring realistic geometries and topographies, to demonstrate that it can be harnessed for use in different applications, including the controlled guidance of micro-cargos, and drags drug delivery in biological environments and other lab-on-a-chip applications, at different spatial scales.[27]

2. Results

2.1. Self-Assembling Micro-structured Substrates

In the search for different strategies to promote the directed transmission of micrometric particles, we are mainly interested in the formation of microstructured tracks preferentially oriented in the direction in which transport is required. On the one hand, the application of a homogeneous magnetic field in the direction parallel to the *X*-axis of the experimental coil system produces self-assembled patterns such as those shown in **Figure 1**A (top row of microscopy photographs, and computer graphic on the left). In a relatively concentrated colloidal suspension of magnetic microsized particles, settled on the water/glass interface after a few minutes, the magnetized particles form large linear assemblies. These assemblies tend to aggregate laterally, and form bands or bundles, with openings, pools, and branches, mainly oriented along the direction imposed by the field.[28] In these structures, the average lateral distance between the different bundles decreases with the surface density of the particles, while the value of their standard deviations is constant and ≈2 microns (Figure 1B, Movie S1, Supporting Information). Alternatively, the application of a high-frequency rotating field in the XZ plane, highly polarized along the X axis, with $\beta^{zx} = \frac{H_z^2 - H_x^2}{H_z^2 + H_x^2} < -0.5$, promotes the formation of more regular patterns (Figure 1A, row of microscopy images below, infographic in center, and Movie S1, Supporting Information). When the rotating field is applied at a frequency high enough so that the translational motion of the particles is negligible during a rotation of the field, the time-averaged interaction between the particles causes the particles to aggregate into dynamic self-assembled structures.[24,29] These are parallel linear chains of rotating microspheres, also parallel to the solid confining boundary, on which discs composed of

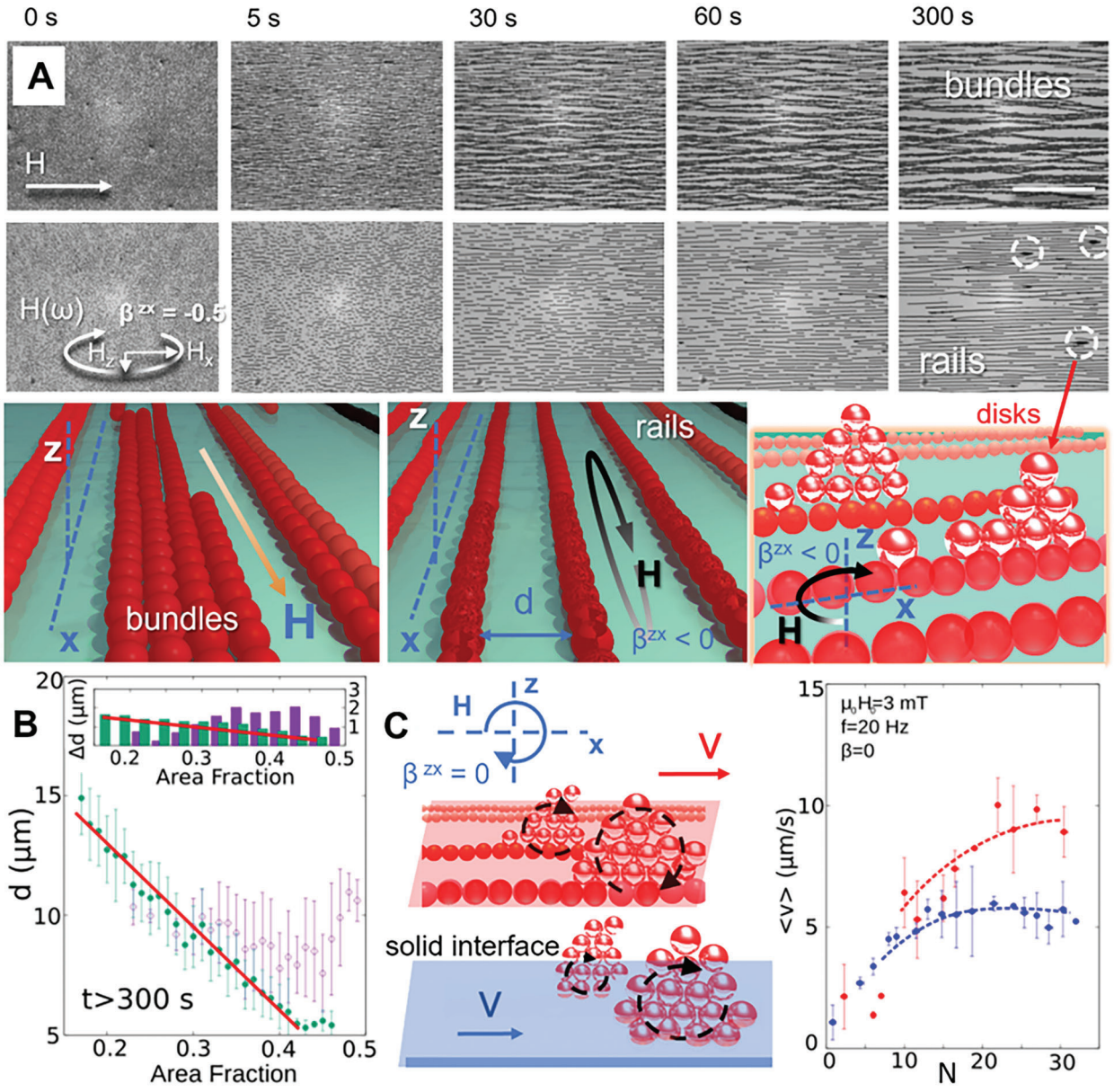

Figure 1. A) (Movie S1, Supporting Information) Self-assembled bundles and chains formed by colloids when energized by a constant ($\mu_0 H_x$ = 1.5 mT, top row of images, and infographics at left) or an elliptically polarized rotating field ($\mu_0 H_0$ = 2 mT, β^{zx} = –0.5, f = 20 Hz, lower row of images, and infographics on the center). The last field configuration favors the formation of discs, composed of several magnetic particles, erected on the induced horizontal rails (circled black lines in the last of the microscopy images below, and bright spheres in infographic on the right). Scale length ≈ 0.25 mm. B) Upon the constant field, the average lateral distance between the different bundles decreases with the surface density of particles, while the value of their standard deviations is constant and ≈2 microns (purple circles in the graph and columns in the inset). When applying the elliptically polarized rotating field, the interchain distance decreases linearly with surface density, with decreasing standard deviations (green dots in the graph and columns in the inset). C) If the linear structures are adsorbed on the solid substrate, and the elliptically polarized rotating field is replaced by a circular one, then the new field promotes the coupled rotation-translation of the discs on the adsorbed particle lanes, which shows an average translation speed (red dots, and upper computer image) up to twice as high as that detected when the same structures are transported on the glass surface (blue dots, and lower computer image). The dashed lines are guides for the eye.

several magnetic particles are fixed and lifted in the vertical direction (Figure 1A, black lines encircled in the row of microscopic images below, and infographic on the right).[30] Upon this field configuration, both the increase in surface density and the repulsion between chains favor regular spacing, so that the inter-chain lateral distance decreases linearly with surface density, with decreasing standard deviations (Figure 1B). Figure 1A also shows that at 300 s and sufficiently high surface densities, a certain proportion of parallel linear structures are able to traverse the entire field of view, i.e., more than 0.5 mm. The fraction of aggregates that are uninterrupted over a distance tends to increase with increasing particle surface density and decreases with distance,

both when a constant or an elliptically polarized rotating field is applied (Figure S1, Supporting Information).

The particles used are superparamagnetic, so the magnetic interactions between the particles disappear as soon as the magnetic field is switched off, and the structures formed disintegrate as soon as the constituent particles diffuse into the medium. To fix the field-induced tracks to the solid substrate, a 20 microliter drop of 1 M NaCl solution is placed in contact with the water reservoir in the vicinity of the open edge of the homemade cell. Diffusion facilitates the salt concentration to grow gradually in the sample, increasing earlier in the vicinity of the open edge. By increasing the concentration of the monovalent electrolyte, the electrostatic repulsion between the particles and the glass substrate is shielded. This allows the particles to approach the substrate and eventually bond by attractive short-range van der Waals interactions, favoring both the adsorption of the preformed microstructures at the solid interface and the formation of permanent aggregates.[31] After ≈30 min, the assembled linear structures became adsorbed, while the self-assembled discs still floated on them. It is important to note that salt-induced physisorption is a rather general mechanism that could work on many different substrates, but not on all. In this respect, the chemical nature of the dispersion medium and the surfaces involved could also determine the strategy used to bind the self-assembled structures to the substrate.

At this point, the highly elliptically polarized rotating field, with $\beta^{zx} < -0.5$, was replaced by a circular one. The increase in β^{zx} was determinant to promote the translational-rotational coupled motion of the non-adsorbed self-assembled discs, both when floating on the non-magnetic glass substrate, and on the adsorbed magnetic chains (see Figure S2, Supporting Information). In the new field configuration, the azimuthal part of the magnetic force increases while the attraction between floating structures and adsorbed rails decreases.[24,30,32] The efficiency of the roto-translation mechanism, which in non-magnetic substrates is based on asymmetric dissipation with the near interface,[33,34] and can be slightly enhanced by the presence of micropatterns,[12] is much more pronounced in the proximity of the magnetic micro-structured substrate. The magnetic microstructured rails facilitate the transport mechanism, and the rotation of microwheels on the self-assembled rails results in up to two-fold enhancement in average translation velocity as compared to that of the structures transported directly on the glass surface. In both cases, it was observed that the velocity of the individual spheres moving close to the corresponding substrate is relatively slow. However, for the set of particles forming discs, the effect becomes cooperative, resulting in a faster translational motion, whereby the velocity increases monotonically with disc size (Figure 1C). Several minutes after increasing the ellipticity of the rotating field, the rotating discs left the field of view and moved toward the edge of the chamber.

2.2. Colloidal Transport on the Attached Self-assembled Structures

Once the above structures have been adsorbed on the glass substrate, the reservoir of the electrolyte solution is removed with the aid of a micropipette and replaced with a drop of ultrapure milli-Q water, which is placed again in contact with the suspension. After 4 to 5 exchanges, performed every 5 min, the medium conditions no longer favor adsorption of the newly incorporated particles, while the assembled structures remain adsorbed due to short-range van der Waals attractive interactions between the particles and the substrate. These structures remained physically adsorbed to the substrate even at a flow rate Q of 4500 µL h^{-1}. In the chamber used, this value corresponds to a viscous stress of ≈0.6 N m^{-2}, which is higher than the physiologically relevant wall shear stress values of between 0.09 and 0.12 N m^{-2}.[13] At this point, an extra drop of a magnetic colloidal suspension is placed on the open edge of the chamber. The newly dispersed particles diffuse through the water, settling and floating on the glass substrate in the vicinity of the previously formed microstructures. Finally, the chamber is closed to minimize the effects of drift movements in the experiments and different magnetic field configurations are applied.

2.2.1. Transport of Isolated Monomers Along the Tracks

The application of a rotating magnetic field magnetizes the adsorbed structures in such a way that an itinerant magnetic potential is generated. Such traveling potential promotes, at low frequency, the synchronous transport of those non-adsorbed particles that previously diffused into the vicinity. In this section, we study the mechanism of transport of isolated magnetic spheres along the edge of the adsorbed structures, by applying a rotating field parallel to the plane of the glass/water interface. Similar phenomenology is observed when the field rotates in the XZ plane, but the nonadsorbed particles are transported over the formed structures, and the processes taking place are less accessible by bright-field microscopy (see Figure S3, Supporting Information).

For a given fixed chain, composed of microparticles of radius a, the shape of the potential acting on the transported particles is highly dependent on their size a'. **Figure 2**A shows the potential felt by magnetic particles of different sizes, calculated using the equations provided in the Supporting Materials. Here, θ_i is the angle between the line joining the centers of the transported sphere and the nearest neighboring sphere i within the chain, and the line perpendicular to the chain passing through the center of the latter (sketch in Figure 2A). The transported particles are allowed to adopt orientations with $-\theta_{max} < \theta_i < \theta_{max}$, $\theta_{max} = \text{asin}(\frac{a}{a+a'})$, so they do not overlap with the particles in the chain. $\theta_{max} = 30$ (47) degrees for particles with $a' = 1.4$ µm ($a' = 0.5$ µm).

The imposed driven motion is due to the magnetic force generated when the particles are delayed with respect to the minima of the traveling potential, which is instantaneously balanced by the drag force. In the synchronous regime, below certain critical frequency f_c, the probability density distribution of the angle φ between the energy minima and the line joining the transported and adjacent particle is centered on negative values, and it is determined by the imposed frequency and thermal fluctuations (Figure S4B, Supporting Information). Particles move coherently with the rotating field from one interstitial to another in the chain, while remain stationary when the rotating field is oriented around the main axis of the chain. In each half cycle of duration $T/2$, where T is the period of the rotating field,

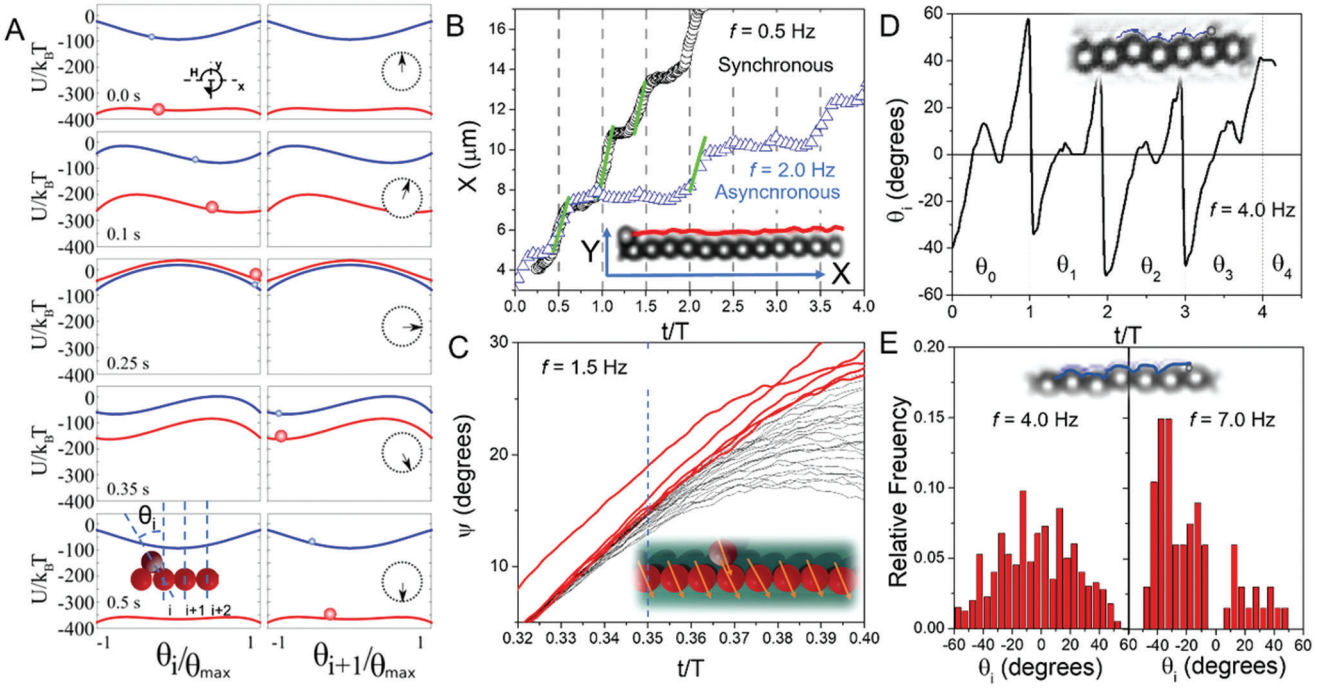

Figure 2. A) Calculated energy potential generated by a long chain of particles with $a = 1.4$ μm, felt by magnetic particles of different sizes, $a' = 0.5$ μm (blue lines, blue spheres) and $a' = 1.4$ μm (red lines, red spheres), for different orientations of the applied rotating field. θ_i is the angle between the line joining the centers of the transported sphere and the nearest neighboring sphere i within the chain, and the line perpendicular to the chain passing through the center of the latter. The $\theta_{max} = 30$ (47) degrees for particles with $a' = 1.4$ μm ($a' = 0.5$ μm). $\beta^{yx} = 0$, $f = 1.0$ Hz and $\mu_0 H = 2$mT. B) X(t) of the transported particles with $a' = 1.4$ μm in the synchronous and the asynchronous regime, with magnetic field amplitude $\mu_0 H = 2$mT, $\beta^{yx} = 0$, $a = 1.4$ μm and frequencies $f = 0.5$ Hz and 2 Hz, respectively. During travel time intervals, the predicted deterministic trajectories are shown as continuous green lines. C) Calculated time evolution of Ψ, the difference between the phase of the potential minimum at $d = a' + a$, $\theta_{i,pot}$, and the phase of the transported particles θ_i, when particles with $a' = 1.4$ μm are transported in the asynchronous regime. Here $a = 1.4$ μm, $\mu_0 H = 2$mT, $\beta^{yx} = 0$ and $f = 1.5$ Hz. D, Movie S4, Supporting Information) Time evolution of θ_i for particles with $a' = 0.5$ μm, $a = 1.4$ μm, $\mu_0 H = 2$mT, $\beta^{yx} = 0$ and $f = 4.0$ Hz. E, Movie S4, Supporting Information) Relative frequency of the values adopted by θ_i when particles with $a' = 0.5$ μm are transported along an adsorbed chain composed of particles with $a = 1.4$ μm, by using a rotating field, $\mu_0 H = 2$mT, $f = 4.0$ Hz (left) and $f = 7.0$ Hz (right).

particles travel for a time interval $t_{travel} = T[\theta_{max}/2\pi]$, only determined by the ratio between the size of the non-adsorbed and adsorbed particles a'/a. In these time intervals, the predicted deterministic trajectories are shown as continuous green lines in Figure 2B. During the range of time when the applied field is oriented approximately along the linear structure, in the time intervals $0.15T < t < 0.30\ T$, or $0.65\ T < t < 0.80\ T$, if the time starts counting when the rotating field is oriented along the positive direction of the Y-axis, the minimum of the accessible potential remains fixed at the orientations in which the particles are located in the interstitials (see the corresponding frames in Figure 2A). Here, the non-adsorbed particles are stopped for a dwell time, to continue the mechanism in the next half cycle, so they travel from one to the closer interstice in each half-field period. Hence, the average linear velocity of the isolated monomers along the direction given by the main axis of the chain is given by $\langle v_x \rangle = 2a/T$. As shown in Figure 2B, the step length given by the particle moving along the X-axis at each half-period is slightly uneven, to some extent altered by the irregularities in the adsorbed linear structures and the slight polydispersity of the adsorbed particles. When the transported particles reach the end of finite chains, they orbit around the last particle due to the magnetic potential generated, like that created by an adsorbed monomer (Figure S4, Supporting Information). Then, the particles continue their translational motion in the opposite direction, the one favored by the rotation of the magnetic field (see Movie S2, Supporting Information).

As the frequency increases, the transported particles gradually lag the generated potential and the probability density distribution of φ becomes broader and shifts toward more negative values. In the asynchronous regime, above the critical frequency f_c, the transported particles are not synchronized with the rotating field, losing the passage of the traveling potential, and their translational motion becomes random. The dynamics of the asynchronous regime are determined by the frequency of the applied field and the size of the transported particles. At frequencies slightly above f_c, the particles with $a' = 1.4$ μm show a perceptible translation every half period (small kinks in Figure 2B), which becomes only occasionally efficient transport (Movie S3, Supporting Information). It is interesting to stress that in this mode, the transported particles do not travel between interstices because fluctuations favored in the direction imposed by the rotating field,[35] but following a deterministic trajectory (green lines in Figure 2B). In Figure 2C, simulation results show that when particles with $a' = 1.4$ μm are transported in the asynchronous regime, $\mu_0 H = 2$ mT and $f = 1.5$ Hz, then Ψ, the difference between the phase of the potential minimum at $a' + a$, $\theta_{i,pot}$, and the phase of the transported particles θ_i, becomes clearly larger in unsuccessful events that in the successful

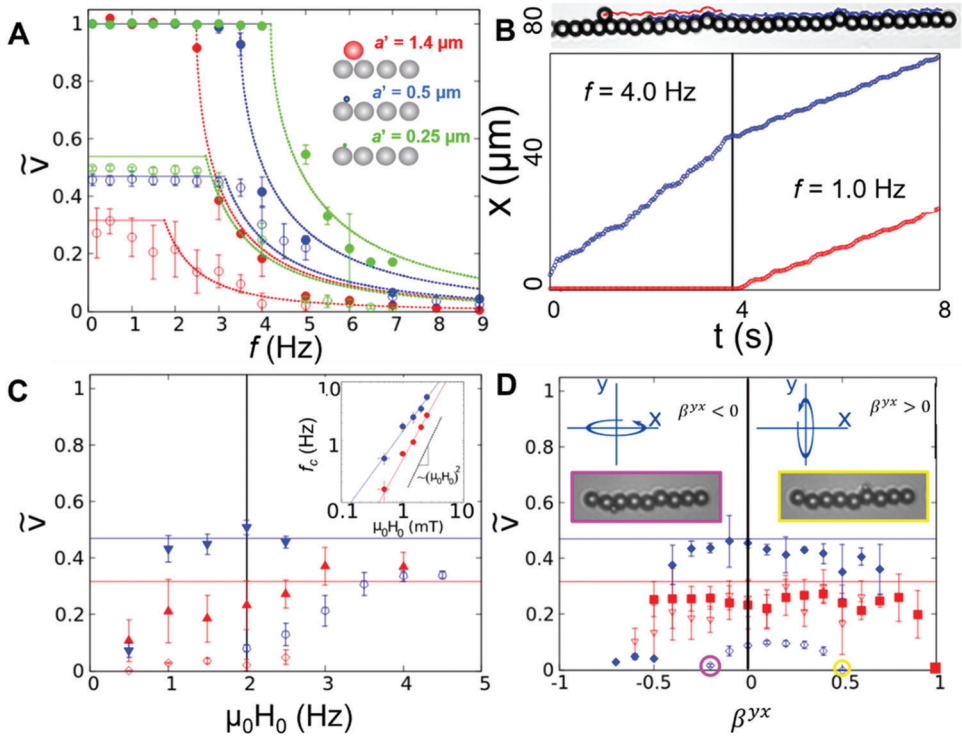

Figure 3. A) Dependence of the reduced linear velocity, $\tilde{v} = (\langle v_x \rangle)/(2\pi(a + a')f)$, with the field frequency f. The field strength is $\mu_0 H = 2$mT, and the ellipticity $\beta^{yx} = 0$ (green, blue, and red circles: spheres with $a' = 0.25$, 0.50, and 1.40 μm orbiting about adsorbed monomers. Blue, green, and red circumferences: particles with $a' = 0.25$, 0.50, and 1.40 μm propelled along adsorbed chains). Dashed lines are commented on throughout the text. B, Movie S5, Supporting Information) When nonadsorbed particles with $a' = 0.50$ and $a' = 1.40$ μm are subjected to a rotating field $\mu_0 H = 2.0$ mT, the change the field frequency, from 4 to 1 Hz, allows them to move from conditions where only the smallest particles are transported to conditions where both types of particles are transported. C) Dependence of $\tilde{v}$ with the field strength (Blue triangle, $a' = 0.50$ and $f = 2.0$ Hz. Red triangle, $a' = 1.40$ and $f = 0.2$ Hz. Blue circumfernece, $a' = 0.50$ and $f = 8.0$ Hz. Red circumfernece, $a' = 1.40$ and $f = 5$ Hz). In the inset, the critical frequency of the particles with $a' = 1.40$ (red dots) and 0.50 μm (blue dots) increases with the field strength as $(\mu_0 H)^b$, being b = 1.87 and 1.42 respectively. D) $\tilde{v}$ as a function of β^{yx}, when $\mu_0 H = 2$mT. Blue circles and circumferences: spheres with $a' = 0.50$ and $f = 2.0$ and 10.0 Hz, respectively. Red squares and triangles: particles with $a' = 1.40$ μm and $f = 0.2$ and 1.0 Hz, respectively. In all the experiments, the adsorbed particles have $a = 1.4$ μm.

ones (those that do not or do promote the translation of the non-adsorbed sphere). Such divergence always emerges in a narrow time interval $0.32 < t/T < 0.38$, when θ_i fluctuates ≈20 degrees and the energy profile of the particle presents the shallowest minima (row 4 in Figure 2A). Since the detachment of the transported particles from the traveling energy minima increases with the drag force, the fraction of half-cycles in which the particles lose the passage of the field increases with the field frequency. At higher frequencies, before coming to a complete stop, particles with $a' = 1.4$ μm also lose a step at larger θ_i values. Particles with $a' = 0.5$ μm, exhibit a different asynchronous mode. At relatively low frequencies, $\mu_0 H = 2$mT and 3.0 Hz < f < 5.0 Hz, the particles lose step regularly (Figure 2D, Movie S4, Supporting Information). During these events, they present forward-backward motion and separate from the chain, as when non-adsorbed particles orbit around adsorbed monomers (Figure S4, Supporting Information),[36] spending more time at θ_i values close to zero. At higher frequencies, $\mu_0 H = 2$ mT and $f \geq 5.0$ Hz, the particles show a kind of mixed mode dynamics, in which the particles lose step every short angular displacements, while tending to remain preferentially stagnant in the interstices for several half cycles, adopting θ_i values below −20 degrees (Figure 2E, Movie S4, Supporting Information). It is important to note that an increase in the viscosity of the fluid will also increase the viscous forces borne by the transported spheres and consequently reduce both the value of the critical frequency at which the particles switch from synchronous to asynchronous transport and the minimum value of the frequency at which transport is interrupted.

Using fixed microstructured substrates composed of particles with $a = 1.40$ μm, we have carried out different series of experiments to study the transport mechanism in more detail, using mobile particles with sizes $a' = 0.25$ μm, $a' = 0.50$ μm, and $a' = 1.40$ μm. It is interesting to note that, in these experiments, the size of the smallest particle is not limited by the transport strategy, but by the magnetic response of the particles and the sensitivity of the bright-field microscope. **Figure 3**A shows the dependence of the reduced linear velocity, defined as $\tilde{v} = \frac{\langle v_x \rangle}{2\pi\,(a+a')\,f}$, with the field frequency, when the field strength is $\mu_0 H = 2$mT, and $\beta^{yx} = 0$. In the synchronous regime, $\tilde{v} = 1$ for the particles orbiting the adsorbed monomers, whereas for particles transported along the adsorbed linear structures $\tilde{v} = 2\,\frac{\theta_{max}}{\pi}$ (horizontal dashed lines in Figure 3A). Among the tested particles, the critical frequency of the particles with $a' = 0.5$ μm is higher than that of the particles with $a' = 1.40$ μm, because in the former the viscous forces are lower, and the magnetic forces are higher. The dependence of

the magnetic forces on the size of the species involved is complex. For an adsorbed chain of particles of a given size, the size of the transported spheres affects the forces generated in two opposite ways. As the size of the nonadsorbed particles decreases, so do their magnetic moments and hence the value of the magnetic energy potentials. On the other hand, their centers get closer to the particles that make up the chain and therefore feel relatively less flat potentials under certain field orientations (see Figure 2A). The two effects have opposite contributions to the magnitude of the magnetic potential gradients, so there is an intermediate size range around half the size of the particles making up the chain where the induced forces are greatest (see Figure S5, Supporting Information). If the size of the transported particles is slightly greater than the size of the particles that make up the chain, they will be far enough from the chain so that, in a certain orientation, they begin to feel a flat potential and therefore no force. Therefore, as confirmed experimentally, the proposed transport strategy becomes inefficient when the size of the non-adsorbed particles is slightly larger than the size of the particles in the substrate.

The dependence of the linear velocity of the particles on the frequency can be correctly set to the Adler equation (curved dashed lines in Figure 3A):

$$\frac{\langle v_x \rangle}{v_{x,max}} = \begin{cases} 1, f < f_c \\ 1 - \sqrt{1 - \left(\frac{f}{f_c}\right)^2}, f > f_c \end{cases} \quad (1)$$

which describes the frequency dependence of the velocity of the transported particle in a stack of different ratchet systems.[36,37] Since the critical frequency is determined, for a given field, by the size and susceptibility of the transported particles, there is a range of frequencies over which a selective transport mechanism can be applied, so that small particles move continuously while large particles remain stationary (see Figure 3B and Movie S5, Supporting Information). On the other hand, the critical frequencies are always lower than the measured value when the particles orbit around a fixed monomer, because when the applied rotating field is oriented in the direction perpendicular to the chain, the traveling potential generated is much shallower than that generated by a monomer (compare the profiles in Figure 2A and Figure S4A, Supporting Information).

The growth in field strength increases the value of the magnetic force exerted and, consequently, increases the maximum viscous drag that particles can overcome before leaving the synchronous regime, Figure 3C. Therefore, the value of the corresponding critical frequency increases with the field strength. In the inset in Figure 3C, the critical frequency of the particles with $a' = 1.4$ and 0.5 μm increases with the field strength as $(\mu_0 H_0)^b$, being $b = 1.87$ and 1.42 respectively. At these critical frequencies, the proportional drag force is close to the maximum magnetic force induced by the traveling potential, and the experimental dependences between f_c and H_0 approximate a squared dependence (as predicted by Equation 6 in the Experimental/Methods Section). On the other hand, Figure 3D shows the dependence of $\tilde{v}$ as a function of the β^{yx}. In all cases studied, including the transport of the discs shown in Figure S2, the mean particle velocity drops abruptly to zero, when β^{yx} (*or* β^{zx}) $< \beta_c = -0.6$. To understand the effect that field polarization has on the efficiency of the mechanism, it is convenient to appreciate that the energy profile generated by the adsorbed chain when β^{yx} (*or* β^{zx}) < -0.6 is much dimmer than that obtained when β^{yx} (*or* β^{zx}) $= 0$ (Figure S6, Supporting Information). Above β_c, the transport is approximately insensitive to β^{yx}, although it obviously drops to zero at $\beta^{yx} = 1$. In the asynchronous regime of the particles of size $a' = 0.5$ μm, the range of beta values where the mechanism promotes transport is strongly reduced, and these non-adsorbed particles are trapped in the cup (interstices) of the chain links for values of $\beta^{yx} > 0.5$ (< -0.2) (inset in Figure 3D).

Finally, we tested the robustness of the transport mechanism in the presence of strong hydrodynamic flows. In the experiments, the 1.0 micron particles, transported on adsorbed chains of 2.4 micron particles under the action of a rotating field of 2.0 mT and a frequency of 0.5 Hz, were able to maintain synchronous mode when a flow was injected into the camera with a caudal $Q > -350$ μL h^{-1}. (the – sign indicates that the flow is in the opposite direction to the direction of particle transport). Below this critical value, which corresponds in the geometry of the containing chamber used to a viscous stresses of 0.04 N m^{-2}, slightly below the physiologically relevant wall shear stress values (0.09–0.12 N m^{-2}), the transported particles often strip off the track (Figure S7, Supporting Information).

2.2.2. Transport of Small Aggregates Along the Tracks

Under semi-dilution conditions, when it is likely to observe the simultaneous meeting of two moving spheres, the applied rotating magnetic field not only promotes the generation of the traveling potential, but also the formation of small aggregates of moving particles.[24] In the remainder of this discussion, we will focus on the behavior of the species formed when the moving particles are equal in size to the particles forming the adsorbed chain, $a = 1.4$ μm. Dimers follow different dynamic behaviors. In the synchronous regime, they usually rotate with the frequency of the applied field around the axis perpendicular to the interparticle vector, traveling a distance $2a$ in one field cycle. During half of the cycle, one of the two spheres beats on the other, which serves as a hinge, transiently attached to the fixed substrate. During the next half of the cycle, the two spheres switch roles, and the tail sphere rolls forward to become the head sphere (**Figure 4**A,I, Movie S6, Supporting Information), in a mechanism that resembles the one adopted by the processive molecular walkers.[38] At low frequencies, the dimers also align and orbit around a particle of the linear chain, synchronously with the applied field (Figure 4A,iii), or glide over the microstructured substrate without showing any rotation (Figure 4A,iv). At higher frequencies, in the asynchronous regime, the dimers can combine the above modes to others in which they rotate about their own axis, on the guiding chain, without showing any translation (Figure 4A,ii). In the case of trimers and tetramers, the system dynamics are again dictated by the imposed magnetic and viscous torques, as well as the interparticle interactions, so that different modes of motion are consistent with those of dimers in the synchronous regime. However, increasing the number of particles involved leads to an even more complex asynchronous regime, where the self-assembled structures rotate and translate asynchronously on the linear structures in a random pattern. For all these species,

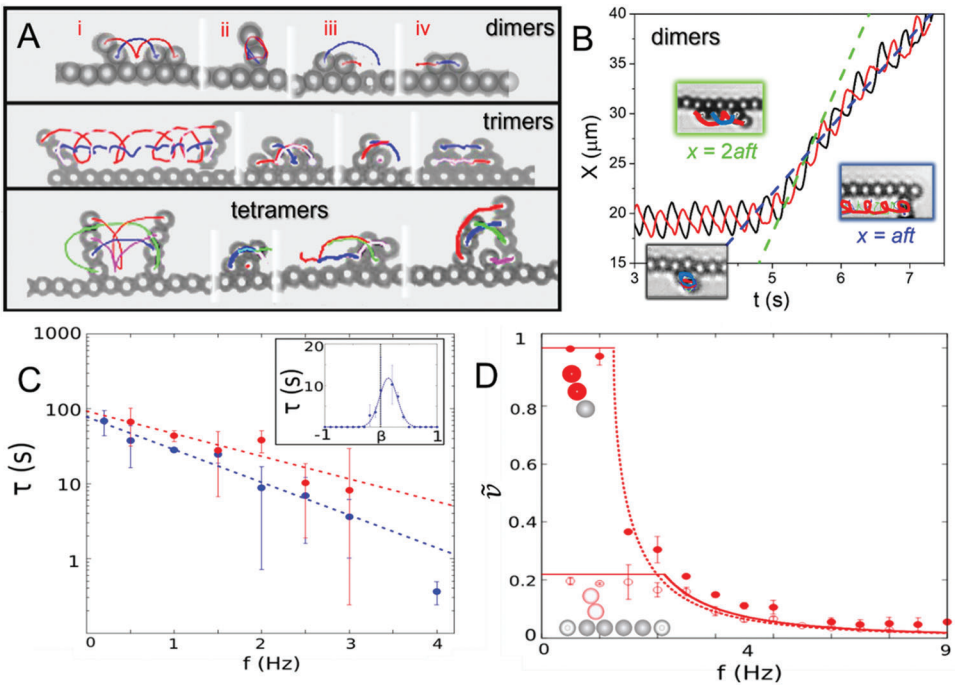

Figure 4. A) i) In the dimers, we observe walkers, ii) static rotors, iii) sliding walkers, and iv) surfers. In the case of trimers and tetramers, different modes of motion are consistent with those of dimers in the synchronous regime. In all these experiments, $\mu_0 H = 2$mT and $\beta^{yx} = 0.0$. For the dimers $f =$ 1.0 Hz. For the trimers $f =$ 1.5 Hz for the first mode, and $f =$ 1.0 Hz for the rest. For the tetramers, $f =$ 0.1 Hz and 1.0 Hz for the compact structures and open structures, respectively. B) The trajectories followed by the particles composing a dimer when transported on a long chain, when $\mu_0 H = 2$mT, $\beta^{yx} =$ 0 and $f =$ 3.0 Hz, show how at these conditions, several dynamic behaviors coexist. The dashed lines are used to visualize the different modes adopted by the dimers. C) Lifetime of moving dimers (blue dots), trimers (red dots) versus field frequency. Dashed lines represent an exponential dependence described by the expression $t_c = t_0 \exp(-f/f_c)$, where f_c is a critical value of the frequency and t_0 is a prefactor with a time dimension. (dimers: $f_c = 1.0$ Hz, $t_0 = 77$s; trimers: $f_c = 1.4$ Hz, $t_0 = 93$ s). Inset: For $\mu_0 H = 2$mT and $f =$ 2.0 Hz, the dimer lifetime shows a maximum close to $\beta^{yx} = 0$. D) $\tilde{v}$ versus f, when a dimer revolves around an isolated monomer (red circles), or when it is transported along an adsorbed rail (red circumferences). Here, $\mu_0 H = 2$mT and $\beta^{yx} = 0$.

several dynamic behaviors can coexist at a given frequency, as they often have similar energy profiles (Figure S8, Supporting Information). In Figure 4B, we show a case in which a dimer begins by showing a rotor-like trajectory, followed by walking-like dynamics in which the dimer travels a distance $2a$ in one field cycle, and a final regime in which the transported particles follow a motion like the previous one, but travel a distance a in one field cycle.

In the absence of irregularities in the linear geometry of the substrate, or the presence of other moving particles, the lifetime of these unstable moving aggregates, defined here as the time required for at least one of their constituent particles to be separated from the rest by at least one particle of the self-assembled substrate, is strongly determined by the field frequency. Figure 4C shows how for the dimers and trimers formed by particles with $a' = 1.4$ μm, the lifetime decreases exponentially with f and is well described by the expression $t_c = t_0 \exp(-f/f_c)$, where f_c is a critical value of the frequency and t_0 is a time dimension prefactor. The exponential dependence reflects the increased tendency of the aggregated particles to jump over the interparticle energy barrier, caused by the hydrodynamic energy, $\eta\dot{\gamma}a^2\delta$. Here, $\dot{\gamma}$ is the hydrodynamic shear rate, η the kinematic viscosity and δ is the microscopic length over which the interparticle attractive potential is effective.[39] This dependence is reminiscent of a thermally activated Arrhenius process, characterized by a tentative rupture frequency and an energy barrier that decreases monotonically with field frequency. As expected, for a given value of the field strength and frequency, the dependence of the dimer lifetime on the field ellipticity shows a maximum close to zero (inset in Figure 4C). On the other hand, the lifetime of transient aggregates decreases drastically when they have 4 or more particles, and under semi-dilution conditions, it is very difficult to detect aggregates composed of more than 3 particles. Figure 4D shows the reduced main velocity of the dimers as a function of field frequency when they rotate around an adsorbed monomer, or when they are transported along an adsorbed rail. In the second case, the synchronous regime covers a wider range of frequencies, also broader than the range measured for the transported monomers (compare with Figure 3A).

2.2.3. Colloidal Currents on Attached Self-Assembled Structures

The combination of all the above strategies, field-induced self-assembly, adsorption, and field-driven transport, allows for the generation of guided colloidal currents along the preformed structures. When the rotating field is applied in the plane parallel to the substrate, the adsorbed parallel bundles, previously formed

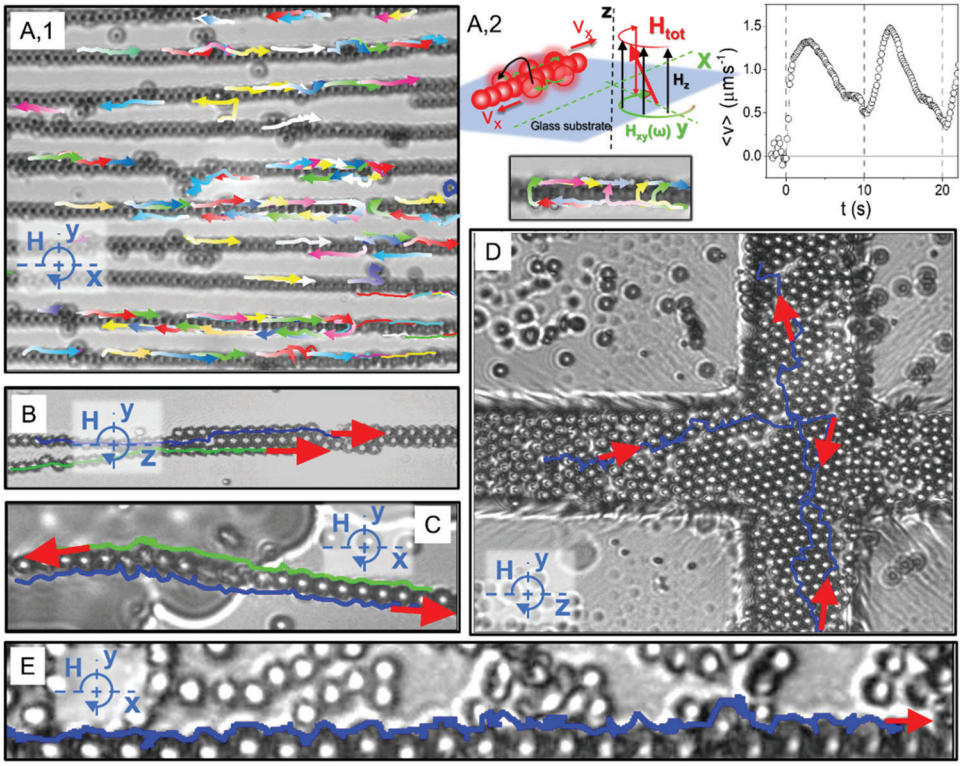

Figure 5. A,1, Movie S8, Supporting Information) The collective transport of particles of size $a' = 0.5$ μm on sets of adsorbed parallel rails, when the rotating field is applied in the XY plane, is induced in opposite directions, which cancels collective transport. A,2) This effect can be easily overcome by applying pulses of helical fields that favor the accumulation of transported particles on only one side of the adsorbed structures, promoting collective transport only in one direction and positive averaged velocity values. The Z pulses locked with the rotating field are applied every 10 s (dashed lines). In all these experiments, $\mu_0 H = 2.0$ mT and $f = 0.5$ Hz. B) When the field rotates in the vertical plane, all particles are transported along the rails and bundles, in the direction imposed by the rotating field $\mu_0 H = 2.0$ mT, $\beta^{zx} = -0.4$, $f = 1$ Hz. (C, Movie S10, Supporting Information) A long chain, adsorbed on a surface with a micro-sized profile, allows two small particles to be transported between two regions of different attitudes $\mu_0 H = 2.5$ mT, $\beta^{yx} = 0, f = 0.2$ Hz. D, Movie S11, Supporting Information) Wall-to-wall adsorbed mats within microfluidic channels, consisting of particles of a relatively concentrated, predried colloidal suspension, serve as the micro-structured magnetic substrate necessary to transport nonadsorbed magnetic particles along preplanned trajectories. The mobile particles are transported on the carpets, and the field conditions are $\mu_0 H_0 = 3.0$ mT, $\beta^{zx} = -0.4, f = 0.5$ Hz. E, Movie S12, Supporting Information) A particle of size $a' = 0.5$ microns is transported over a glass surface while surrounded by a relatively large number of adsorbed and non-adsorbed non-magnetic spheres $\mu_0 H_0 = 2.0$ mT, $\beta^{yx} = 0, f = 1$ Hz.

by a constant magnetic field, presents some drawbacks for the collective transport of particles. The latter is severely limited by the presence of branches or puddles, where particles change their direction of motion or remain confined (Figure S9, Movie S7, Supporting Information). Parallel rails do not have these limitations, but in principle, they may have others, such as the presence of holes in the layout or undulations in the linear geometry of the structures (**Figure 5**A,1, Movie S8, Supporting Information). The latter rarely pose a serious obstacle to the driven transport of the particles, since they involve only a slight delay, as the non-adsorbed spheres are able to adapt to non-linear profiles (Figure S10,i, Supporting Information). The former favor the reversal of the driven motion of the particles, but are sometimes overcome by small aggregates, capable of jumping over the defects to maintain their direction of motion (Figure S10,ii, Supporting Information). One aspect that greatly limits the collective transport induced by rotating fields oriented parallel to the substrate, when driven on bundles or parallel rails, is that the particles move along opposite directions on both sides of the adsorbed structures, so that the biased movements are averaged to give no net directionality (Figure S10,iii, Supporting Information). In the case of parallel rails, this limitation can be easily overcome by applying field pulses along the vertical, locked to the in-plane rotating field. During the application of vertical pulses, T/2 every 20 cycles of the rotating field, the total field and the promoted magnetic moments process around the vertical axis passing through the center of the particles (Figure 5A2). The resulting magnetic torques promote the movement of the non-adsorbed particles out of the resting plane and their jump onto the adsorbed tracks. The field pulses, however, induce particle jumps only on one side of the parallel tracks, since the downward helical motion of the counterparts is prevented by the presence of the solid substrate. As soon as the vertical pulse is turned off, the field rotates again in the plane parallel to the substrate and the non-adsorbed particles continue their driven motion in the direction parallel to the linear structures. After the pulse, the number of particles on both sides of the chains is unbalanced and transport in one direction is favored. Figure 5A,2 shows how after the application of a pulse along Z, the measured average velocity of the particles adopts values different from zero. The intensity of the promoted uncompensated

currents decreases in time due to the presence of defects, but increases after the application of each pulse, which in the experiment shown are applied every 10 s.

When the field rotates in the vertical plane, both tracks and bundles are still useful for induced transport (Movie S9, Figure 5B, and S2, Supporting Information). In this configuration, particles are more difficult to detect by bright microscopy, but they are all transported along the same direction. The promoted structures can also adsorb on surfaces with a micro-sized topography, so that the driving particles are able to overcome the vertical and explore irregular orography and steep profile. Figure 5C (Movie S10, Supporting Information) shows the trajectories of two small particles transported along a long chain linking two regions of different elevations. These regions were created by melting 5 micron-sized polystyrene particles, previously dried on the glass substrate (Figure S11, Supporting Information). Various controlled drying or patterning strategies can also be adopted to fill ad hoc microfluidic channels with a dense monolayer of magnetic colloids. Adsorbed wall-to-wall carpets will subsequently serve as the micro-structured magnetic substrate needed to transport non-adsorbed magnetic particles along preplanned trajectories (Figure 5D, Movie S11, Supporting Information). Finally, it should be noted that the driven mechanism is also capable of inducing transport along crowded environments. Figure 5E, Movie S12, Supporting Information, shows the trajectory of a driven particle of size $a' = 0.5$ microns, which is transported along a surface containing a relatively high density of adsorbed and non-adsorbed non-magnetic spheres. In all the processes described throughout the article, the direction of motion is easily reversed by simply reversing the direction of rotation of the applied field. Besides, the driven particles are easily released at the target site, since both adsorbed structures and charges are superparamagnetic, and their magnetic interactions can be instantly canceled by switching off the applied magnetic field.

3. Conclusion

The self-assembly capability of magnetically responsive colloids opens the door to their use as track-building units on which other magnetic particles can be guided and, consequently, to the development of a new class of colloidal materials, bringing together the widely explored fields of colloidal self-assembly and magnetic micromanipulation. The proposed design mimics the transport strategies adopted by many biomachines subjected to induced power strokes, such as kinesin, which are associated with self-assembled tracks through noncovalent interactions to reduce the available degrees of freedom and walking.[6] In the described approach, the formation of the self-assembled tracks first requires the transport and adsorption of the building blocks at the sites where driving motion is required. This limiting step can be accelerated by applying a field gradient, i.e., by bringing a magnet close to the building blocks to attract them and force their diffusion and sedimentation in the vicinity of the target site. Alternatively, self-assembled planar or linear structures can be brought into the target environment by methods based on the controlled generation of hydrodynamic flows, such as coupled roto-translational mechanisms.[30,34,40] The latter type of strategy, which is effective when the size and the magnetic moment of the rotated particles are sufficiently large, could then be incorporated into the first step of the protocol described in the manuscript, which is in principle more suitable for the controlled and rapid transport of swarms of smaller particles.

The main innovation, with respect to the other strategies already adopted for the transport of matter at the microscale, is that the self-assembled structures serving as conveyor tracks can be adapted ad hoc to the properties of the environment in which the micro-objects are to be transported. The described strategy, extremely versatile, can also be adopted directly for the transport of matter at smaller nanoscale, provided that the magnetic energies involved are higher than the thermal energy, but also at macroscale, when the materials composing the rails and the transported particles have a soft magnetization. The knowledge gained on the proposed drive mechanism will allow the design of functional systems with tailor-made structures from first principles, with the ability to guide moving particles through preplanned trajectories and irregular profiles. These advances will allow the development of new materials that respond to stimuli and adapt to the environment, with novel functionalities and applications in the field of bioengineering.

In principle, there are a number of technological areas where the strategy described could have direct applications, including in biological environments. In vitro, perhaps the most straightforward is the possibility of building smart microfluidic chips with lab-on-a-chip applications such as microfluidic control or cell transport, handling, and characterization.[41] As shown in Figure 5D, predesigned channels can be filled with adsorbed magnetic particles which act as attachment points for the driven and selective transport of non-adsorbed magnetic particles, even in the absence of externally generated flows. On the other hand, the proposed strategy is in principle directly applicable to stagnant or low-velocity fluidic biological environments, such as the gastrointestinal tract, the peritoneal cavity, or the interior of the eye. Besides, as noted above (Figure S7, Supporting Information), the locomotion strategy could also be advantageous for upstream locomotion and thus in areas of the human body with significant fluid flow, such as the circulatory/vascular system, which is typically the ideal route to reach the target site. This is because the strategy is based on the use of colloids adsorbed to vessel walls, where flow velocities are typically lower. Hence, the experimental approach described provides an alternative to the use of microrollers, which have to some extent demonstrated a large upstream locomotion capability in veins and arteries.[13] However, unlike microrollers, the proposed strategy is in principle not limited in small vessels by confinement effects[42] or by the surface microtopographies found in the inner walls of blood vessels.[43]

In the next future, we plan to implement alternative micropatterning methods,[44] in addition to exploring the possibility of transport along trajectories outside the confining plane. In this sense, magnetic membranes, foams, or magnetic chains linked through different polymeric bridges could help to enhance three-dimensional transport and overcome the limitations imposed by gravity in different applications.[26,45] On the other hand, the described methodology is of fundamental interest, as it could help to understand the role of the power stroke and Brownian ratchet mechanism in motor protein transport,[40] along with other cooperative and non-equilibrium effects: the

control of the effect of hydrodynamic interactions arising between microrotors, the occurrence of synchronous and bound states in colloidal swarms, the study of hydrodynamic boundary states in viscous media, of dense jammed and/or confined systems, or the use of such systems as active probes in bulk or interfacial microrheological measurements.[46] The latter are pressing and urgent issues that must be addressed to understand the mechanical properties of micro-structured biological systems.

4. Experimental Section

For the construction of self-assembled architectures and their visualization by video-microscopy techniques, colloidal suspensions are confined in a sealed chamber, 1.5 mm wide, 2 cm long, and 80 μm high, which helps to minimize convective movements. The suspension is introduced by capillary action between a glass slide (RS) and a coverslip (Menzel-Glaser), spaced with two parallel rectangular adhesive tapes. Then, one of the open edges is sealed with 200 mPa silicone oil (Sigma Aldrich), and the other remains open to a reservoir of water. The latter helps to prevent the sample from drying out during the process while allowing the exchange of medium conditions and the introduction of new particles. The magnetic particles gradually settle to the bottom of the chamber due to the density difference with the external medium. After sedimentation, the particles remain suspended at some distance from the slide surface, due to the equilibrium between the gravitational force and the repulsive electrostatic interaction between the substrate and the particles, both negatively charged.

In this work, we use a commercial aqueous suspension of superparamagnetic spherical particles, Dynabeads M−270 and Myone (Invitrogen), and PS-MAG-COOH Particles (micro-particles GmbH). The beads are composed of a polystyrene matrix doped with nanometric superparamagnetic grains of iron oxides (Fe_2O_3 and Fe_3O_4). Dynabeads M−270, with a radius $a = 1.4$ μm, are monodisperse, with a variation coefficient CV less than 3%, have a density $\rho_{\text{particle}} = 1.8$ g cm^{-3}, a magnetic susceptibility under a static field $\chi = 0.91$, in the range of 0–5 mT, and are stabilized with carboxylic groups at the surface. Dynabeads MyOne, supplied by Invitrogen (USA), are 1.0 μm in diameter, monodisperse (CV < 5%), with identical composition, a magnetic susceptibility under a static field $\chi = 1.62$, in the range of 0–5 mT, and also stabilized with carboxylic groups (see Figure S12, Supporting Information).[47,48] Before preparing them at the required experimental conditions, the commercial colloidal suspensions are washed twice in pure water.

The chamber containing the sample is placed in the center of a set used to generate the magnetic fields: two pairs of insulated copper wire coils oriented along the *X* and *Y*-axes, facing each other at a distance equal to their diameter, and a third coil oriented along the *z*-axis, all placed in the vicinity of the microscope stage (Figure S13, Supporting Information). The signal feeding the coils is created with a signal generator (National Instruments 9269, USA) connected to three current amplifiers (KEPCO, bipolar power supply/operating amplifier, USA). By modulating the amplitude and frequency of the current, different magnetic fields can be applied. The actuated system is monitored with an upright optical microscope (Nikon Eclipse 80-I with a working distance of 50 × objective, 0.25NA, Japan) connected to a CCD camera (Edmund, EO 1312-M), that allows imaging of the system with single-particle resolution. The chosen range of frame rate values, between 10 and 100 ms, allows to calculate the particle velocity during the whole process.

In the construction of the microchannels used in Figure 5D, the glass substrate was precleaned with isopropyl alcohol and deionized water. The water was then desorbed by heating it at 100° for 1 min. Next, the positive photoresist AZ4533 was deposited, using a centrifuge at 1500 rpm for 30 sec. The system was gently baked at 100° for 50s and exposed to an ultraviolet lamp for 22 s. Finally, the sample was introduced into AZ826MF developer liquid for ≈1 min.

To study out-of-plane transport along the self-assembled structures, 5.7-micron non-magnetic particles were placed on an Invitrogen glass slide and left to dry for one day. Once the particles were physically adsorbed on the substrate, we heated the sample in the oven for 2 h at 180 °C, and preheated for 30 min at 180 °C. The molten particles form an irregular orography and a steep relief. Before use, we waited 10 min to cool the sample.

In the experiments carried out for monitoring the adhesion of the adsorbed particles and the response of the transport strategy in the presence of hydrodynamic flows (Figure S7, Supporting Information), the chamber in which the particles are adsorbed is connected to a pump. The pump consists of an external pressure source, and a compressor, connected to the pressure regulator (OB1 MK4, microfluidic flow controller, ELVEFLOW). The controller is connected to a pressurized reservoir of Milli-Q water, the fluid used, which in turn is connected to a flow sensor via a microfluidic tube. Finally, the water flow is directed to the homemade prismatic microfluidic cell.

In the numerical simulations, we have used a homemade modification of LAMMPS simulation package.[49] We have restricted the whole system to the *XY* plane. We consider the motion of a particle of diameter σ' on a chain formed by particles of diameter $\sigma = 2.8\ \mu m$. These particles are not time-integrated to fix its position, but they are able to interact with the moving spheres. The equation of motion of the particle in translation is given by the usual Langevin equation of overdamping for Brownian motion

$$\frac{d\vec{r}}{dt} = -\frac{1}{\gamma}\vec{\nabla}U + \sqrt{2\frac{k_B T}{\gamma}}\ \vec{\xi} \tag{2}$$

where $\vec{r}$ is the position of the moving particle, $U(\vec{r})$ is the pair interaction potential energy, γ is the friction coefficient, $T = 298\ K$ is the bath temperature and $\vec{\xi}$ is a two-component vector with each component being an independent Gaussian random variable, i.e., namely, $\langle \xi_\alpha(t)\rangle = 0$ and $\langle \xi_\alpha(t)\ \xi_\beta(t')\rangle = \delta_{\alpha\beta}\ \delta(t-t')$. The interaction between particles is given by two contributions: The magnetic interaction between the induced dipoles of each particle due to the magnetic field and the excluded volume. For the latter, we have used a soft pure repulsive potential, WCA,

$$U(r) = 4\epsilon''\left[\left(\frac{\sigma''}{r}\right)^{12} - \left(\frac{\sigma''}{r}\right)^{6} + \frac{1}{4}\right] \quad \left(r > 2^{\frac{1}{6}}\sigma''\right) \tag{3}$$

with σ'' related to the distance between interacting particles and ϵ'' related with the smoothness of the potential. Since we have different particle sizes, these parameters have been chosen by the usual mixing rule for mixtures, $\sigma'' = \frac{\sigma+\sigma'}{2}$ and $\epsilon'' = \sqrt{\epsilon\ \epsilon'}$. On the other hand, the magnetic interaction has been calculated from the expression for the energy between two magnetic dipoles:

$$U_{ij} = -\frac{\mu_0}{4\pi}\left[\frac{3\left(\overrightarrow{m_i}\cdot\overrightarrow{r_{ij}}\right)\left(\overrightarrow{m_j}\cdot\overrightarrow{r_{ij}}\right)}{r_{ij}^5} - \frac{\left(\overrightarrow{m_i}\cdot\overrightarrow{m_j}\right)}{r_{ij}^3}\right] \tag{4}$$

where $\mu_0 = 4\pi 10^{-7}\ A\cdot s/(V\cdot m)$ is the magnetic permeability of vacuum, $\overrightarrow{m_i}$ is the particle i-th dipole and $r_{ij} = |\vec{r_j} - \vec{r_i}|$ is the relative distance between particles. The inter-particle force derived from this energy is given by:

$$\overrightarrow{F_{ij}} = \frac{3\mu_0}{4\pi r_{ij}^5}\left[\left(\overrightarrow{m_i}\cdot\overrightarrow{r_{ij}}\right)\overrightarrow{m_j} + \left(\overrightarrow{m_j}\cdot\overrightarrow{r_{ij}}\right)\overrightarrow{m_i} + \left(\overrightarrow{m_i}\cdot\overrightarrow{m_j}\right)\overrightarrow{r_{ij}} - \frac{5\left(\overrightarrow{m_i}\cdot\overrightarrow{r_{ij}}\right)\left(\overrightarrow{m_j}\cdot\overrightarrow{r_{ij}}\right)}{r_{ij}^2}\overrightarrow{r_{ij}}\right] \tag{5}$$

Since the system consists of super-paramagnetic particles in the presence of a global magnetic field $\overrightarrow{B_0} = \mu_0\overrightarrow{H_0}$, the magnetic dipole induced in an isolated particle is given by $\overrightarrow{m_i} = \chi_i\ V_i\overrightarrow{H_0}$, where we have considered the susceptibility of an ideal, isotropic, homogenous particle χ_i; and V_i is the volume of the particle. Both quantities have been chosen as in experiments. In the proximity of other particles, the mutual induction between particles must be considered, and the magnetic dipole of each particle becomes $\overrightarrow{m_i} = \chi_i V_i(\overrightarrow{H_0} + \vec{H}_{int,i})$. Hence, considering magnetic fields as

$\overrightarrow{H_0} = H_0\,\hat{h}$, the dipole with first-order correction due to the local magnetic field is given by:

$$\overrightarrow{m_i} \approx \chi_i\, V_i\, H_0 \left\{ \hat{h} + \frac{\chi_i V_i}{4\pi} \sum_{j\neq i} \left[\frac{3\left(\hat{h}\cdot\overrightarrow{r_{ij}}\right)}{r_{ij}^5}\overrightarrow{r_{ij}} - \frac{\hat{h}}{r_{ij}^3} \right] \right\} \tag{6}$$

In our experiments, the direction of the magnetic field changes in time as $\hat{h}(t) = (\cos(2\pi f_x t),\ \sin(2\pi f_y t))$. Note that for the system under consideration here, this first-order correction is ≈10% of the total value of the magnetic dipole.

Supporting Information

Supporting Information is available from the Wiley Online Library or from the author.

Acknowledgements

The authors thank Eduardo Guzmán and Laura Rodríguez Arriaga for fruitful discussions. The C.A.I. de Espectroscopia y Correlación and the C.A.I. de Técnicas Físicas, both of the Universidad Complutense de Madrid, are thanked for their availability for the use of their facilities. This work was funded by Ministerio de Ciencia e Innovacion (Grants No. PID2019-105343GB-I00, PID2019-106557GB-C21 and PID2022-140407NB-C21).

Conflict of Interest

The authors declare no conflict of interest.

Data Availability Statement

The data that support the findings of this study are available from the corresponding author upon reasonable request.

Keywords

colloids, driven transport, magnetic materials, self-assembly

Received: June 9, 2023
Revised: July 20, 2023
Published online: September 3, 2023

[1] M. J. Skaug, C. Schwemmer, S. Fringes, C. D. Rawlings, A. W. Knoll, *Science* **2018**, *359*, 1505.
[2] a) H. Ceylan, J. Giltinan, K. Kozielski, M. Sitti, *Lab Chip* **2017**, *17*, 1705; b) M. Sitti, H. Ceylan, W. Hu, J. Giltinan, M. Turan, S. Yim, E. Diller, *Proc. IEEE Inst. Electr. Electron. Eng.* **2015**, *103*, 205; c) B. J. Nelson, I. K. Kaliakatsos, J. J. Abbott, *Annu. Rev. Biomed. Eng.* **2010**, *12*, 55.
[3] L. Hines, K. Petersen, G. Z. Lum, M. Sitti, *Adv. Mater.* **2017**, *29*, 1603483.
[4] E. M. Purcell, *Am. J. Phys.* **1977**, *45*, 3.
[5] R. Iino, K. Kinbara, Z. Bryant, *Chem. Rev.* **2020**, *120*, 1.
[6] S. Erbas-Cakmak, D. A. Leigh, C. T. McTernan, A. L. Nussbaumer, *Chem. Rev.* **2015**, *115*, 10081.
[7] L. Chen, M. Nakamura, T. D. Schindler, D. Parker, Z. Bryant, *Nat. Nanotechnol.* **2012**, *7*, 252.
[8] J. B. Konrad, S. Roland, M. Peter, U. Eberhard, *Nanotechnology* **2001**, *12*, 238.
[9] a) M. von Delius, E. M. Geertsema, D. A. Leigh, *Nat. Chem.* **2010**, *2*, 96; b) S. Kassem, T. van Leeuwen, A. S. Lubbe, M. R. Wilson, B. L. Feringa, D. A. Leigh, *Chem. Soc. Rev.* **2017**, *46*, 2592.
[10] M. Driscoll, B. Delmotte, *Curr. Opin. Colloid Interface Sci.* **2019**, *40*, 42.
[11] F. Martínez-Pedrero, P. Tierno, *J. Colloid Interface Sci.* **2018**, *519*, 296.
[12] a) G. Wang, X. Li, X. Tan, S. Ji, J. Huang, H. Duan, P. Lv, *Adv. Intell. Syst.* **2021**, *3*, 2000226; b) T. Yang, A. Tomaka, T. O. Tasci, K. B. Neeves, N. Wu, D. W. M. Marr, *Sci. Rob.* **2019**, *4*, eaaw9525.
[13] Y. Alapan, U. Bozuyuk, P. Erkoc, A. C. Karacakol, M. Sitti, *Sci. Rob.* **2020**, *5*, eaba5726.
[14] J. L. Abbott, A. V. Straube, D. G. A. L. Aarts, R. P. A. Dullens, *New J. Phys.* **2019**, *21*, 083027.
[15] P. Tierno, S. V. Reddy, J. Yuan, T. H. Johansen, T. M. Fischer, *J. Phys. Chem. B* **2007**, *111*, 13479.
[16] H. Gu, E. Hanedan, Q. Boehler, T.-Y. Huang, A. J. T. M. Mathijssen, B. J. Nelson, *Nat. Mach. Intell.* **2022**, *4*, 678.
[17] a) F. Martínez-Pedrero, F. Ortega, R. G. Rubio, C. Calero, *Adv. Funct. Mater.* **2020**, *30*, 2002206; b) H. Massana-Cid, A. Ortiz-Ambriz, A. Vilfan, P. Tierno, *Sci. Adv.* **2020**, *6*, eaaz2257.
[18] H. Massana-Cid, F. Meng, D. Matsunaga, R. Golestanian, P. Tierno, *Nat. Commun.* **2019**, *10*, 2444.
[19] a) B. B. Yellen, O. Hovorka, G. Friedman, *Proc. Natl. Acad. Sci. USA* **2005**, *102*, 8860; b) P. Tierno, F. Sagués, T. H. Johansen, T. M. Fischer, *Phys. Chem. Chem. Phys.* **2009**, *11*, 9615.
[20] a) B. Wang, Y. Zhang, Z. Guo, L. Zhang, *Mater. Today* **2019**, *25*, 112; b) S. H. L. Klapp, *Curr. Opin. Colloid Interface Sci.* **2016**, *21*, 76.
[21] L. Rossi, in *Frontiers of Nanoscience*, (Eds: D. Chakrabarti, S. Sacanna), Elsevier, Netherlands, **2019**, Vol. *13*, p. 1.
[22] F. Martinez-Pedrero, A. Cebers, P. Tierno, *Phys. Rev. Appl.* **2016**, *6*, 034002.
[23] S. K. Smoukov, S. Gangwal, M. Marquez, O. D. Velev, *Soft Matter* **2009**, *5*, 1285.
[24] F. Martínez-Pedrero, A. González-Banciella, A. Camino, A. Mateos-Maroto, F. Ortega, R. G. Rubio, I. Pagonabarraga, C. Calero, *Small* **2021**, *17*, 2101188.
[25] a) R. Dreyfus, J. Baudry, M. L. Roper, M. Fermigier, H. A. Stone, J. Bibette, *Nature* **2005**, *437*, 862; b) X. Chen, L. Zhang, *Microchim. Acta* **2017**, *184*, 3639; c) X. Zhang, J. Guo, X. Fu, D. Zhang, Y. Zhao, *Adv. Intell. Syst.* **2021**, *3*, 2000225.
[26] A. Grein-Iankovski, A. Graillot, M. Radiom, W. Loh, J.-F. Berret, *J. Phys. Chem. C* **2020**, *124*, 26068.
[27] a) J. D. G. Durán, J. L. Arias, V. Gallardo, A. V. Delgado, *J. Pharm. Sci.* **2008**, *97*, 2948; b) Y. Dai, L. Jia, L. Wang, H. Sun, Y. Ji, C. Wang, L. Song, S. Liang, D. Chen, Y. Feng, X. Bai, D. Zhang, F. Arai, H. Chen, L. Feng, *Small* **2022**, *18*, 2105414; c) B. J. Nelson, P. Dupont, D. Floreano, K. Goldberg, H. Gu, N. Jacobstein, C. Laschi, H. Lipson, *Sci. Rob.* **2022**, *7*, eade5834; d) M. B. Akolpoglu, Y. Alapan, N. O. Dogan, S. F. Baltaci, O. Yasa, G. Aybar Tural, M. Sitti, *Sci. Adv.* **2022**, *8*, eabo6163.
[28] J. Faraudo, J. S. Andreu, C. Calero, J. Camacho, *Adv. Funct. Mater.* **2016**, *26*, 3837.
[29] J. E. Martin, A. Snezhko, *Rep. Prog. Phys.* **2013**, *76*, 126601.
[30] F. Martinez-Pedrero, A. Ortiz-Ambriz, I. Pagonabarraga, P. Tierno, *Phys. Rev. Lett.* **2015**, *115*, 138301.
[31] J. Martín-Roca, M. Jiménez, F. Ortega, C. Calero, C. Valeriani, R. G. Rubio, F. Martínez-Pedrero, *J. Colloid Interface Sci.* **2022**, *614*, 378.
[32] A. Mateos-Maroto, F. Ortega, R. G. Rubio, C. Calero, F. Martínez-Pedrero, *Phys. Rev. Appl.* **2021**, *16*, 064045.
[33] T. O. Tasci, P. S. Herson, K. B. Neeves, D. W. M. Marr, *Nat. Commun.* **2016**, *7*, 10225.

[34] C. E. Sing, L. Schmid, M. F. Schneider, T. Franke, A. Alexander-Katz, *Proc. Natl. Acad. Sci. USA* **2010**, *107*, 535.
[35] A. V. Straube, P. Tierno, *Europhys. Lett.* **2013**, *103*, 28001.
[36] G. Helgesen, P. Pieranski, A. T. Skjeltorp, *Phys. Rev. Lett.* **1990**, *64*, 1425.
[37] R. R. Agayan, R. G. Smith, R. Kopelman, *J. Appl. Phys.* **2008**, *104*, 054915.
[38] C. L. Asbury, A. N. Fehr, S. M. Block, *Science* **2003**, *302*, 2130.
[39] J. Guery, E. Bertrand, C. Rouzeau, P. Levitz, D. A. Weitz, J. Bibette, *Phys. Rev. Lett.* **2006**, *96*, 198301.
[40] F. Martinez-Pedrero, P. Tierno, *Phys. Rev. Appl.* **2015**, *3*, 051003.
[41] a) S. Tottori, L. Zhang, F. Qiu, K. K. Krawczyk, A. Franco-Obregón, B. J. Nelson, *Adv. Mater.* **2012**, *24*, 811; b) L. Zhang, K. E. Peyer, B. J. Nelson, *Lab Chip* **2010**, *10*, 2203.
[42] U. Bozuyuk, A. Aghakhani, Y. Alapan, M. Yunusa, P. Wrede, M. Sitti, *Nat. Commun.* **2022**, *13*, 6289.
[43] U. Bozuyuk, H. Ozturk, M. Sitti, *Adv. Intell. Syst.* 2300099, https://doi.org/10.1002/aisy.202300099.
[44] a) J. E. Song, J. S. Park, B. Lee, S. B. Pyun, J. Lee, M. G. Kim, Y. Han, E. C. Cho, *Adv. Mater. Interfaces* **2018**, *5*, 1800138; b) E. D'Arcangelo, A. P. McGuigan, *BioTechniques* **2015**, *58*, 13; c) S. G. Moorjani, L. Jia, T. N. Jackson, W. O. Hancock, *Nano Lett.* **2003**, *3*, 633; d) L. Loren, J. S. Russell, *Nanotechnology* **2000**, *11*, 47.
[45] a) C. Goubault, F. Leal-Calderon, J.-L. Viovy, J. Bibette, *Langmuir* **2005**, *21*, 3725; b) T. Yang, T. O. Tasci, K. B. Neeves, N. Wu, D. W. M. Marr, *Langmuir* **2017**, *33*, 5932; c) T. Yang, B. Sprinkle, Y. Guo, J. Qian, D. Hua, A. Donev, D. W. M. Marr, N. Wu, *Proc. Natl. Acad. Sci. USA* **2020**, *117*, 18186; d) R. Mhanna, Y. Gao, I. Van Tol, E. Springer, N. Wu, D. W. M. Marr, *Langmuir* **2022**, *38*, 5730; e) T. Yang, D. W. M. Marr, N. Wu, *Colloids Surf. A* **2018**, *540*, 23; f) J. Byrom, P. Han, M. Savory, S. L. Biswal, *Langmuir* **2014**, *30*, 9045; g) H. Singh, P. E. Laibinis, T. A. Hatton, *Nano Lett.* **2005**, *5*, 2149.
[46] a) D. Lips, R. L. Stoop, P. Maass, P. Tierno, *Commun. Phys.* **2021**, *4*, 224; b) A. J. Mendoza, E. Guzmán, F. Martínez-Pedrero, H. Ritacco, R. G. Rubio, F. Ortega, V. M. Starov, R. Miller, *Adv. Colloid Interface Sci.* **2014**, *206*, 303.
[47] D. T. Grob, N. Wise, O. Oduwole, S. Sheard, *J. Magn. Magn. Mater.* **2018**, *452*, 134.
[48] G. Fonnum, C. Johansson, A. Molteberg, S. Mørup, E. Aksnes, *J. Magn. Magn. Mater.* **2005**, *293*, 41.
[49] A. P. Thompson, H. M. Aktulga, R. Berger, D. S. Bolintineanu, W. M. Brown, P. S. Crozier, P. J. in 't Veld, A. Kohlmeyer, S. G. Moore, T. D. Nguyen, R. Shan, M. J. Stevens, J. Tranchida, C. Trott, S. J. Plimpton, *Comput. Phys. Commun.* **2022**, *271*, 108171.
[50] X. J. A. Janssen, A. J. Schellekens, K. van Ommering, L. J. van Ijzendoorn, M. W. J. Prins, *Biosens. Bioelectron.* **2009**, *24*, 1937.